Miner Deposita (2014) 49:861–877
DOI 10.1007/s00126-014-0522-7

ARTICLE

Mineralisation of amethyst-bearing geodes in Ametista do Sul (Brazil) from low-temperature sedimentary brines: evidence from monophase liquid inclusions and stable isotopes

H. Albert Gilg · Yves Krüger · Heinrich Taubald · Alfons M. van den Kerkhof · Martin Frenz · Giulio Morteani

Received: 18 December 2013 / Accepted: 1 April 2014 / Published online: 4 May 2014

Abstract Fluid inclusion studies in combination with hydrogen, oxygen and sulphur isotope data provide novel insights into the genesis of giant amethyst-bearing geodes in Early Cretaceous Paraná continental flood basalts at Amestita do Sul, Brazil. Monophase liquid inclusions in colourless quartz, amethyst, calcite, barite and gypsum were analysed by microthermometry after stimulating bubble nucleation using single femtosecond laser pulses. The salinity of the fluid inclusions was determined from ice-melting temperatures and a combination of prograde and retrograde homogenisation temperatures via the density maximum of the aqueous solutions. Four mineralisation stages are distinguished. In stage I, celadonite, chalcedony and pyrite formed under reducing conditions in a thermally stable environment. Low $\delta^{34}S_{V\text{-}CDT}$ values of pyrite (−25 to −32‰) suggest biogenic sulphate reduction by organotrophic bacteria. During the subsequent stages II (amethyst, goethite and anhydrite), III (early subhedral calcite) and IV (barite, late subhedral calcite and gypsum), the oxidation state of the fluid changed towards more oxidising conditions and microbial sulphate reduction ceased. Three distinct modes of fluid salinities around 5.3, 3.4 and 0.3 wt% NaCl-equivalent characterise the mineralisation stages II, III and IV, respectively. The salinity of the stage I fluid is unknown due to lack of fluid inclusions. Variation in homogenisation temperatures and in $\delta^{18}O$ values of amethyst show evidence of repeated pulses of ascending hydrothermal fluids of up to 80–90 °C infiltrating a basaltic host rock of less than 45 °C. Colourless quartz and amethyst formed at temperatures between 40 and 80 °C, while the different calcite generations and late gypsum precipitated at temperatures below 45 °C. Calculated oxygen isotope composition of the amethyst-precipitating fluid in combination with δD values of amethyst-hosted fluid inclusions (−59 to −51‰) show a significant ^{18}O-shift from the meteoric water line. This ^{18}O-shift, high salinities of the fluid inclusions with chloride-sulphate composition, and high $\delta^{34}S$ values of anhydrite and barite (7.5 to 9.9‰) suggest that sedimentary brines from deeper parts of the Guaraní aquifer system must have been responsible for the amethyst mineralisation.

Keywords Amethyst · Monophase fluid inclusions · Retrograde homogenisation · Density maximum · Hydrogen isotopes · Sulphur isotopes · Sedimentary brines

Editorial handling: B. Lehmann

H. A. Gilg (✉)
Lehrstuhl für Ingenieurgeologie, TUM, Arcisstr. 21, 80333 Munich, Germany
e-mail: agilg@tum.de

Y. Krüger · M. Frenz
Institut für Angewandte Physik, Universität Bern, Sidlerstrasse 5, 3012 Bern, Switzerland

H. Taubald
Lehrstuhl für Isotopengeochemie, Universität Tübingen, Wilhelmstrasse 56, 72074 Tübingen, Germany

A. M. van den Kerkhof
Angewandt Geologie, Universität Göttingen, Goldschmidtstr. 3, 37077 Göttingen, Germany

G. Morteani
Hydroisotop GmbH, Woelkestrasse 9, 85301 Schweitenkirchen, Germany

Introduction

Amethyst, a valuable gemstone of the quartz family, owes its purple colour to the presence of tetravalent iron in the crystal lattice (e.g. Rossman 1994). Deposits of amethyst thus require a source of silica, a precipitation mechanism preferably at relatively low temperatures in order to avoid high aluminium

contents and the formation of smoky quartz, oxidising conditions to incorporate Fe^{3+}, and finally a source of radiation to transform Fe^{3+} to Fe^{4+}. Therefore, most amethysts are hosted by siliceous felsic rocks rich in radioactive elements, such as K, U and Th. The precipitation of quartz occurs at shallow crustal levels, where hydrothermal fluids can mix with oxidising meteoric waters (Gilg 2012). Nevertheless, the largest and economically most significant amethyst deposits of the world (Baretto and Bittar 2010) occur within a kilometer-thick pile of predominately basaltic lava flows of the Paraná-Etendeka Continental Flood Basalt (CFB) Province in southern Brazil (Ametista do Sul) and Uruguay (Artigas), i.e. in rocks with low silica and radioactive element concentrations and a reducing, Fe^{2+}-dominated environment.

A solution to this paradox was given by Gilg et al. (2003), who proposed that colourless quartz and amethyst in the geodes did not precipitate from hydrothermal solutions during the cooling of the basaltic lavas, but from upwelling, oxidised meteoric waters of the Guaraní aquifer that underlies the basalts. The huge Guaraní aquifer formed several tens of millions of years after the eruption of the lavas as a consequence of regional climatic and tectonic changes. The study stimulated new research on the Brazilian and Uruguayan amethyst deposits (e.g. Proust and Fontaine 2007a, b; Juchem et al. 2009; Duarte et al. 2009, 2011; Commin-Fischer et al. 2010; Morteani et al. 2010; Hartmann et al. 2010, 2012a, b; Rosenstengel and Hartmann 2012).

Ongoing discussions mostly consider (a) the origin of the cavities (Proust and Fontaine 2007a; Duarte et al. 2009; Hartmann et al. 2012a, b) and (b) the temperature, composition and source of the fluids involved in the mineralisation of the geodes (Proust and Fontaine 2007b; Morteani et al. 2010; Hartmann et al. 2012a).

Most authors consider the cavities as large vesicles of accumulated magmatic gas (e.g. Gilg et al. 2003; Proust and Fontaine 2007a; Morteani et al. 2010). However, this view has been recently challenged. Duarte et al. (2009) interpreted the cavities as epigenetic voids formed by hydrothermal leaching, whereas the same research group in later publications (Hartmann et al. 2012a, b) rather assumed ballooning of a boiling fluid phase in argillically altered, soft basalts. We consider both epigenetic hydrothermal models of cavity formation not convincing, as they cannot explain the hydrodynamic shapes of the geodes with upward convex bases and skirted rims (e.g. Fig. 9 in Morteani et al. 2010) as well as their occurrence in defined levels within the lava flows. Furthermore, similarly shaped, but unfilled domed megavesicles are known from unaltered pahoehoe lavas of the Columbia River CFB Province (McMillan et al. 1987; Thordarson and Self 1998) and from the recent basaltic lava flows at Surtsey (Thordarson and Sigmarsson 2009). Thus, the formation of such megavoids in similar positions within the lava flows does not require hydrothermal activity, but is a primary magmatic degassing phenomenon.

The temperature, composition and origin of the mineralising fluids responsible for the geode infill are less well constrained. Proust and Fontaine (2007b) found exclusively aqueous two-phase (liquid–vapour) inclusions in amethyst with homogenisation temperatures of 152 to 238 °C and salinities of 0.9 to 2.6 wt% NaCl-equivalent, and interpreted them as of magmatic origin, whereas all other studies described assemblages of monophase all-liquid inclusions and only rarely individual liquid–vapour inclusions (Juchem 1999; Gilg et al. 2003; Commin-Fischer et al. 2010; Morteani et al. 2010; Duarte et al. 2011). The homogenisation temperatures of two-phase inclusions reported in these studies do not yield consistent results and scatter from 66 to 229 °C probably indicating leakage and/or necking (Commin-Fischer et al. 2010). Due to the presence of predominately monophase inclusions and referring to the work of Goldstein and Reynolds (1994), the temperature of geode infill was estimated to be below 100 °C. Salinity determinations were hampered by the absence of a vapour bubble during ice melting in almost all inclusions and may also have been influenced by leakage and evaporation. Some studies reported ice-melting temperatures in the presence of vapour between −1 and 0 °C (Gilg et al. 2003; Duarte et al. 2011), while others showed larger ranges from −7.5 to 0.0 °C with several modes (Juchem 1999; Commin-Fischer et al. 2010). The involvement of meteoric waters was favoured by all these studies.

Stable isotope studies revealed significant isotope variations for oxygen in macrocrystalline quartz (Borget 1980; Juchem 1999; Juchem et al. 2009; Duarte et al. 2011), for carbon in calcite (Gilg et al. 2003; Morteani et al. 2010; Duarte et al. 2011) and for sulphur in sulphate and altered wall rocks (Gilg et al. 2003; Duarte et al. 2011). The interpretation of these large isotope variations in terms of temperature or isotopic variations of the fluid, changes in oxidation state or isotopically distinct sources in the case of carbon and sulphur remains unclear. No hydrogen isotope studies on geode minerals or fluid inclusions have yet been published, but are important to evaluate the role of meteoric water in the mineralisation.

Our petrographic studies include microscopy in transmitted and reflected light as well as cathodoluminescence microscopy. The latter method may provide information on the growth textures in the quartz, which are indicative of the forming conditions.

We present a new method of measuring the salinity and density of monophase liquid inclusions in amethyst, calcite, barite and gypsum from the Ametista do Sul area. Single ultrashort pulses of a tightly focussed femtosecond laser were used to stimulate vapour bubble nucleation and thus transferring the metastable liquid inclusions to stable liquid–vapour inclusions appropriate for subsequent microthermometric measurements (Krüger et al. 2007). This technique allows us to determine the

salinity and homogenisation temperature of initially monophase inclusions that previously could not be analysed by microthermometry. The fluid inclusion study is complemented by a preliminary D/H study on fluid inclusions in amethyst and stable hydrogen and oxygen isotope analyses on gypsum water to determine the origin of waters involved in the mineralisation. Finally, we present some new sulphur isotope measurements on sulphides and sulphates within the amethyst geodes.

Geological setting and paragenesis

The Paraná-Etendeka large igneous province consists of a preserved volume of about 1.7 Mio km³ (Frank et al. 2009) of mostly basaltic and subordinate rhyodacitic to rhyolitic volcanic rocks. Recent geochronological data including U-Pb isotope data on zircon indicate a relatively short eruption period of 1 to 2 m.y. about 135 Ma ago (Thiede and Vasconcelos 2010; Pinto et al. 2011). These data contradict the previous view of a more protracted extrusion history that is based exclusively on ^{40}Ar-^{39}Ar ages on feldspar (e.g. Turner et al. 1994; Stewart et al. 1996). The Early Cretaceous lavas of the Serra Geral Formation cover an up to 3,000-m-thick Paleozoic to Mesozoic sedimentary sequence of the intracratonic Paraná basin (Zalan et al. 1991; Mariani et al. 2013) that hosts the large Guaraní aquifer system at its top (Araújo et al. 1999; Morteani et al. 2010). The lavas are covered by Late Cretaceous terrestrial sediments of the Bauru Group (Goldberg and Garcia 2000). Continental-scale meteoric water flow in the Guaraní aquifer started as a consequence of the rift shoulder uplift on the Brazilian Atlantic coast side (Serra Geral, Serra do Mar) and a climatic change from arid to seasonally humid in the Late Cretaceous (Araújo et al. 1999). Significant block faulting of the lava pile along NW-striking lineaments with vertical displacements of up to 200 m has been documented in the Ametista do Sul region (Rosenstengel and Hartmann 2012). Tertiary to Quaternary uplift and erosion has brought the deposits to the surface.

The two major amethyst mining districts are Ametista do Sul, northern Rio Grande do Sul, Brazil, and Artigas or sometimes named "Los Catalanes gem field", northern Uruguay. They are located in distinct stratigraphic positions within the 1.7-km-thick lava pile of the Serra Geral Formation (Fig. 1). The main amethyst deposits in the Ametista do Sul mining area are hosted in a Ti-rich Pitanga-type basaltic lava flow located about 1,000 m above the base of the volcanic sequence (Gilg et al. 2003; Rosenstengel and Hartmann 2012), while in Artigas the amethyst geodes are hosted in Ti-poor Gramado-type basalts situated near the base of the flood basalt pile (Morteani et al. 2010; Hartmann et al. 2010). The Palaeozoic to Mesozoic sediments underlying the lavas reach a thickness of about 1,500 to 2,000 m (Mariani et al. 2013). At both sites, the amethyst-bearing geodes are hosted at

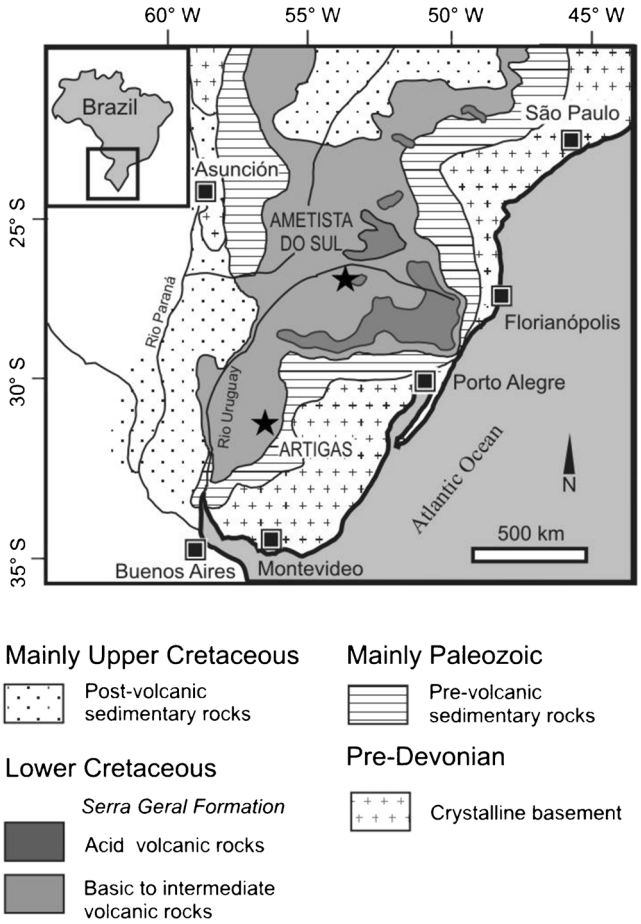

Fig. 1 Geological overview map showing the Paraná basin and location of the amethyst mining districts of Ametista do Sul, Brazil, and Artigas, Uruguay (from Gilg et al. 2003)

a specific level within the upper part of 30 to 50 m thick basaltic pahoehoe lavas and have a similar though not identical paragenetic sequence of geode infill.

^{40}Ar-^{39}Ar dating of celadonite (Vasconcelos 1998) and Sr-isotope studies on calcite (Gilg et al. 2003) from the Ametista do Sul area indicate that the geode infill started 20 to 30 million years after basalt eruption and lasted more than 10 million years during Late Cretaceous times. Even younger, Tertiary ages have been suggested recently for the formation of agates in the Paraná basalts (Moxon et al. 2013). In some geodes, a brecciation of early silica and subsequent cementation by later silica precipitates can be observed, which indicates that the mineralisation occurred during times of brittle tectonic activities and/or under conditions of hydraulic fracturing (e.g. Duarte et al. 2009).

Materials and methods

Samples were collected from several underground mines in the Ametista do Sul area (see Gilg et al. 2003); *coordinates*

and sample numbers are given in brackets: Angico (*W53 16 07.0;S 29 06 21.0*; 15386), Bortoluzzi (*W53 18 45.9;S 27 19 06.7*; 15369), Celio (*W53 12 54.1;S 27 20 35.5*; 15288, 15289), Elio Zanon (*W53 18 41.5;S 27 18 50.9*; 15343, 15344), Mioto (*W53 19 05.3;S 27 25 13.1*; 15329) Salles (*W53 09 54.6;S 27 23 00.5*; 15253, 15276, 15279), Simonetti (*W53 20 11.7;S 27 17 52.0*; 15361), and Testa (*W53 06 29.3;S 27 21 08.4*; 15308, 15310, 15311, 15318, 15319).

Sulphides in polished sections were investigated in reflected light using a Leica DM LM polarising microscope at TUM, Munich, and by scanning electron microscopy with EDX at University of Trento, Italy. Mineral purity was also controlled by powder X-ray diffraction analysis using a Phillips PW1800 diffractometer.

A Simon-Neuser HC-3-LM hot cathode (Neuser et al. 1995) equipped with a Kappa DX 40C peltier cooled camera was used for the cathodoluminescence (CL) studies on amethyst, chalcedony and calcite.

Microthermometric measurements were performed using a Linkam THMSG 600 heating/freezing stage mounted on an Olympus BX51 microscope. Amethyst, calcite and barite crystals were cut to sections of 200–400 μm thickness and polished on both faces, whereas slices of the gypsum crystals were obtained by cleaving them along {010}.

Single amplified pulses from a Ti:sapphire femtosecond laser system (Coherent) were used to induce vapour bubble nucleation in the initially monophase liquid inclusions. The laser beam (wavelength 800 nm) is coupled into the microscope through an Olympus UD-P dual port adapter equipped with an XF 2033 dichroic mirror (Omega Opticals) and focused on the sample by a long working distance objective (Olympus LMPlanFL 100/0.8). This setup that is described in detail in Krüger et al. (2007) allows to repeatedly and efficiently induce vapour bubble nucleation in selected fluid inclusions at different temperatures and under microscopic observation. Subsequent microthermometric measurements can be performed without moving the sample. The reproducibility of the T_h measurements is generally within 0.1 °C, indicating that the high intensity laser pulses do not cause any volume changes of the inclusions.

Additionally, selected fluid inclusions were analysed by Raman spectroscopy at HKB (Bern, Switzerland) using a Renishaw InVia Raman spectrometer equipped with a 300 mW diode-type laser (Renishaw HP NIR785) for excitation at 785 nm and a 24 mW Ar-Laser (Spectra-Physics) for excitation at 514 nm.

Sulphur from sulphides and sulphates was converted to SO_2 in sealed tin capsules using an on-line NC 2500 elemental analyser (CarloErba) with combustion temperatures of 1,050 °C and a separation column temperature of 100 °C (Giesemann et al. 1994). The isotope ratios were measured using a Finnigan Delta + XL mass spectrometer and reported as delta values relative to Vienna Cañon Diablo Troilite (V-CDT). The precision and reproducibility of $\delta^{34}S_{V\text{-}CDT}$ values is estimated at about ±0.3‰ as monitored by repeated measurements of international standards (NBS-123, NBS-127 and IAEA-S-3).

Water was extracted off-line from fluid inclusion-bearing amethyst by crushing in stainless steel tubes or by thermal decrepitation at 900 °C in quartz glass tubes, while gypsum hydration water was extracted by heating in vacuum at 450 °C for 1 h. Following a cryogenic separation, water was converted to hydrogen in sealed quartz tubes at 500 °C using zinc and analysed in a Finnigan MAT 252 mass spectrometer (see Baatartsogt et al. 2007 for further analytical details). Oxygen isotope ratios of gypsum hydration water were determined by micro-equilibration with CO_2 (O'Neil and Epstein 1966). Oxygen was extracted from two amethyst crystals using a laser fluorination technique (Sharp 1990; Baatartsogt et al. 2007). Oxygen and hydrogen isotope ratios are reported in the delta notation relative to V-SMOW.

Results

Petrography

Changes in the mineral association supported by stable isotope data and microthermometry define four stages of geode infill (Fig. 2).

Stage I: Celadonite, chalcedony and pyrite

The rim of the geodes is coated by greenish clay minerals dominated by celadonite and in part also expandable clay minerals, including saponite and nontronite (Meunier et al. 1988; Proust and Fontaine 2007b; Commin-Fischer et al. 2010). The green rim is followed by partly banded microcrystalline quartz (chalcedony or agate). Sulphides are locally found in stage I and have not been studied in detail so far. Microscopic inspection reveals that slightly anisotropic pyrite is the only sulphide present in the geodes (Fig. 3a, b, d) with the exception of very rare chalcocite veinlets in a sample from the Bortoluzzi mine (Fig. 3d). Pyrite crystallised mostly into open space and is sometimes inter-grown with chalcedony (Fig. 3b). Euhedral pyrite crystals are occasionally brecciated and cemented by chalcedony. More rarely, the sulphide replaced ilmenite laths at the contact to the basalt (Fig. 3a). The presence of Fe^{2+}-sulphides clearly indicates a reducing environment during stage I of the geode mineralisation.

Oscillating complex CL patterns are observed for chalcedony (Fig. 4e, f) and we note that large variations in trace element contents, including Al and Fe, are reported for chalcedony (Commin-Fischer et al. 2010). Similar CL patterns were described for agate geodes from acidic volcanic rocks (Götze et al. 1999). Rare calcite is found in association with

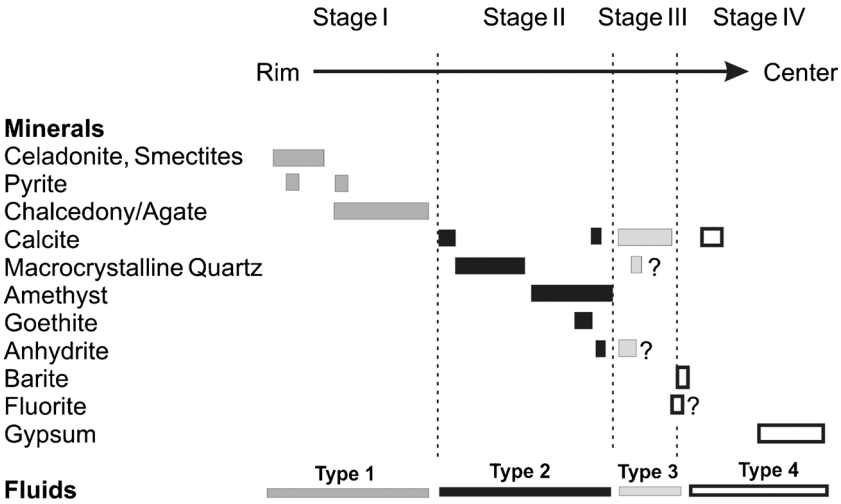

Fig. 2 Paragenetic sequence with four stages of mineral precipitation and related fluid types in amethyst-bearing geodes at Ametista do Sul, Brazil

celadonite and chalcedony and has initially been interpreted as very early stage I carbonate (Gilg et al. 2003; Commin-Fischer et al. 2010). This calcite has a bright red CL colour that is typical for the late stage carbonates (stage III and IV). Microthermometric results (see below) confirm that this calcite formed late in the paragenetic sequence.

Stage II: Amethyst, goethite and anhydrite

The second mineralisation stage of macrocrystalline colourless and amethystine quartz with frequent inclusions of Fe^{3+}-minerals (goethite) and locally sulphates (anhydrite) indicates a redox change towards more oxidising conditions. Sulphides have never been observed during or after the stage II mineralisation. Microscopy with polarized light and hot CL investigations reveal that macroscopic quartz including amethyst shows intense Brazil twinning and strong sector zoning of the rhombohedral planes (Fig. 4a, b, c, d), but no obvious oscillatory growth zonation that would indicate large temperature fluctuations or cyclic compositional variations of the mineralizing fluid during quartz precipitation. The variation of trace element concentrations in macrocrystalline quartz is smaller than in chalcedony (Juchem 1999; Commin-Fischer et al. 2010). The quartz shows patchy short-lived bluish and bright red CL which can be explained by variations in trace element concentrations. Even when trace elements have not been analysed in the present study, it can be assumed that the red CL correlates with Fe^{3+} in the quartz crystal lattice (Müller 2000).

Anhydrite, the earliest sulphate phase is rare but sometimes occurs as tiny tabular inclusions in amethyst or as pinkish silicified sheaths with lengths of more than 10 cm (Fig. 3e; Lieber 1985). Anhydrite was unambiguously identified by Raman spectroscopy and powder X-ray diffraction analysis. Gypsum inclusions have not been observed in quartz. We note that anhydrite is the stable calcium sulphate phase at temperatures exceeding 58 °C (Hardie 1967; Blount and Dickson 1973). The minimum temperature for anhydrite precipitation, however, largely depends on the salinity of the solution and to a minor extent on the fluid pressure. The presence of anhydrite is a valuable temperature indicator for stage II.

Radial fibrous goethite is the predominant iron oxide phase embedded in amethyst from Ametista do Sul. In addition, Commin-Fischer et al. (2010) reported on tiny inclusions of fluorite in macrocrystalline quartz. Early stage II calcite crystals were sometimes found in voids at the base of macrocrystalline quartz and as micro-inclusions in amethyst (Gilg et al. 2003). Finally, we note that the sequence celadonite-chalcedony and macrocrystalline quartz is sometimes repeated. In the rare second sequence, however, no sulphide, sulphate or Fe minerals have been observed.

Stage III: Early subhedral calcite

Large subhedral calcite crystals with various habits (Balzer 2003) are found on top of the amethyst crystals. This first generation of post-amethyst calcites is characterised by heavy carbon isotopes and highly variable oxygen isotope compositions (Gilg et al. 2003).

Stage IV: Late subhedral calcite, gypsum and barite

The latest mineralisation phase deposited on macrocrystalline quartz and subhedral stage III carbonates is represented by late subhedral calcites with very low $\delta^{13}C$ and constantly high $\delta^{18}O$ values, and by large, up to several decimetres long, subhedral clear gypsum crystals (Juchem 1999; Gilg et al. 2003). Occasionally, tabular barite (Juchem 1999) and spherical whitish fluorite aggregates (Pöllmann 2010) on amethyst have been reported. Microthermometric data from a single

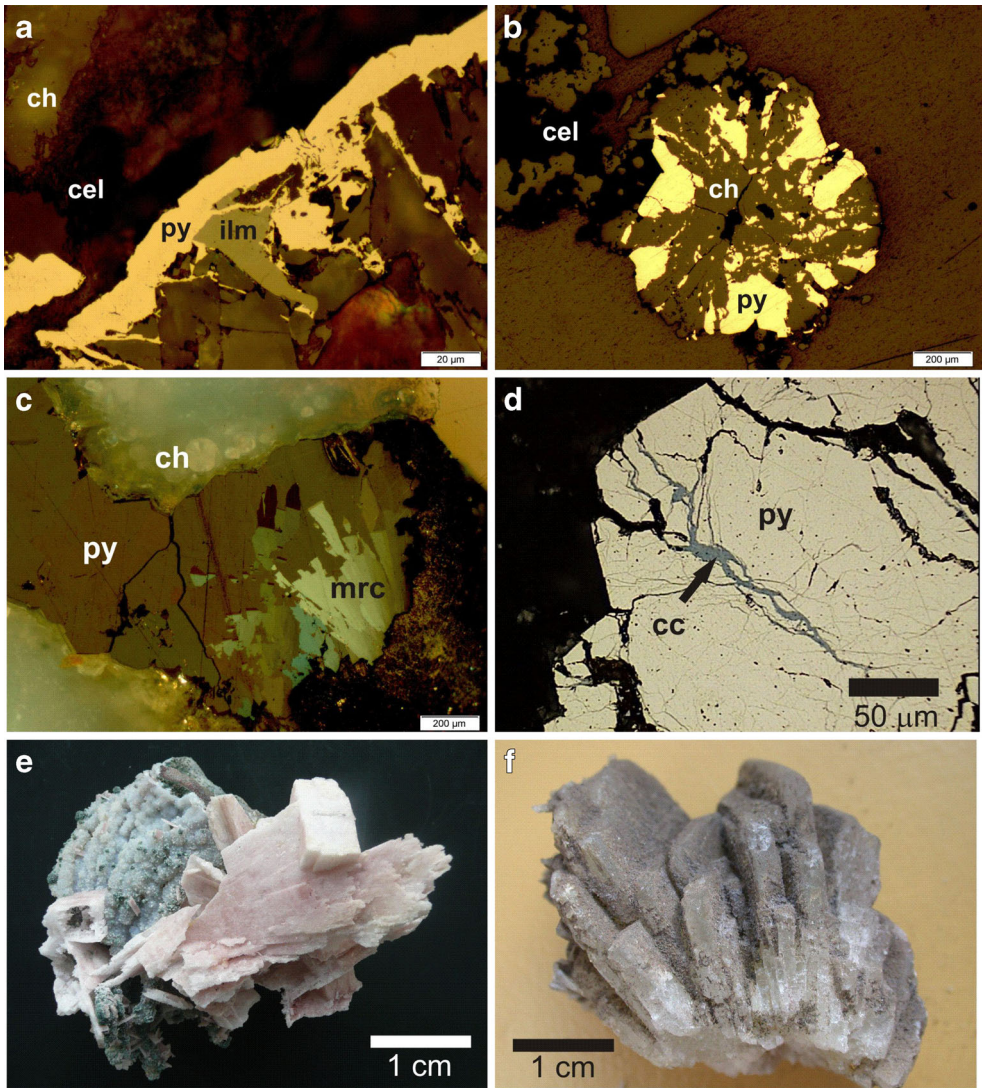

Fig. 3 Sulphides and sulphates in amethyst-bearing geodes. **a** Pyrite (py) crystallised into the cavity, partly replacing ilmenite (ilm) of the basaltic host rock; in association with chalcedony (ch) and celadonite (cel) (sample 15344, reflected polarized light), **b** Spherical chalcedony–pyrite aggregate (sample 15369, reflected polarized light), **c** anisotropic subhedral marcasite (mrc) inclusion in pyrite from Artigas (sample 15834, reflected crossed polarized light). **d** chalcocite (cc) veinlets in fractured pyrite (sample 15369, reflected polarized light), **e** silicified anhydrite crystals (sample Anh-1; Ametista do Sul), **f** tabular barite aggregate (sample 15329)

barite crystal (Fig. 3f) show that barite formed from the same fluid as gypsum and stage IV calcite.

Fluid inclusions

Fluid inclusions were found only in the minerals of stages II, III and IV, but not in stage I minerals. Therefore, the present fluid inclusion study does not provide information on the earliest mineralising fluid(s) (type 1), associated with the precipitation of celadonite, chalcedony and sulphides. A total of more than 500 fluid inclusions were investigated by microthermometry, approximately two thirds hosted in colourless quartz and amethyst and one third hosted in calcite, barite and gypsum crystals. The inclusions are generally monophase liquid, except for very few two-phase inclusions in colourless quartz and amethyst crystals. In quartz and amethyst, the fluid inclusions mainly occur along healed pseudo-secondary and secondary fractures. Primary fluid inclusions are rare and the lack of visible crystal growth zones hampers a clear classification of the inclusion assemblages with respect to crystal growth.

After inducing bubble nucleation in the metastable state of the monophase liquid inclusions using femtosecond laser pulses, we were able to measure prograde (upon heating) and retrograde (upon cooling) liquid–vapour homogenisation temperatures T_h and T_{hr}, respectively. Retrograde liquid–vapour homogenisation, i.e., the homogenisation upon cooling is a consequence of the density maximum of water, resulting in a second intersection of the isochores with the liquid–vapour saturation curve or its metastable extension at negative temperatures (see Fig. 7). Retrograde homogenisation can be observed only in high-density aqueous inclusions, where T_{hr} (L+V→L) is higher than the temperature of ice nucleation ($T_n$ice). Note that T_n(ice) was observed typically between −32 and −41 °C. The relation between T_h and T_{hr} is determined by the concentration and the composition of the dissolved salt

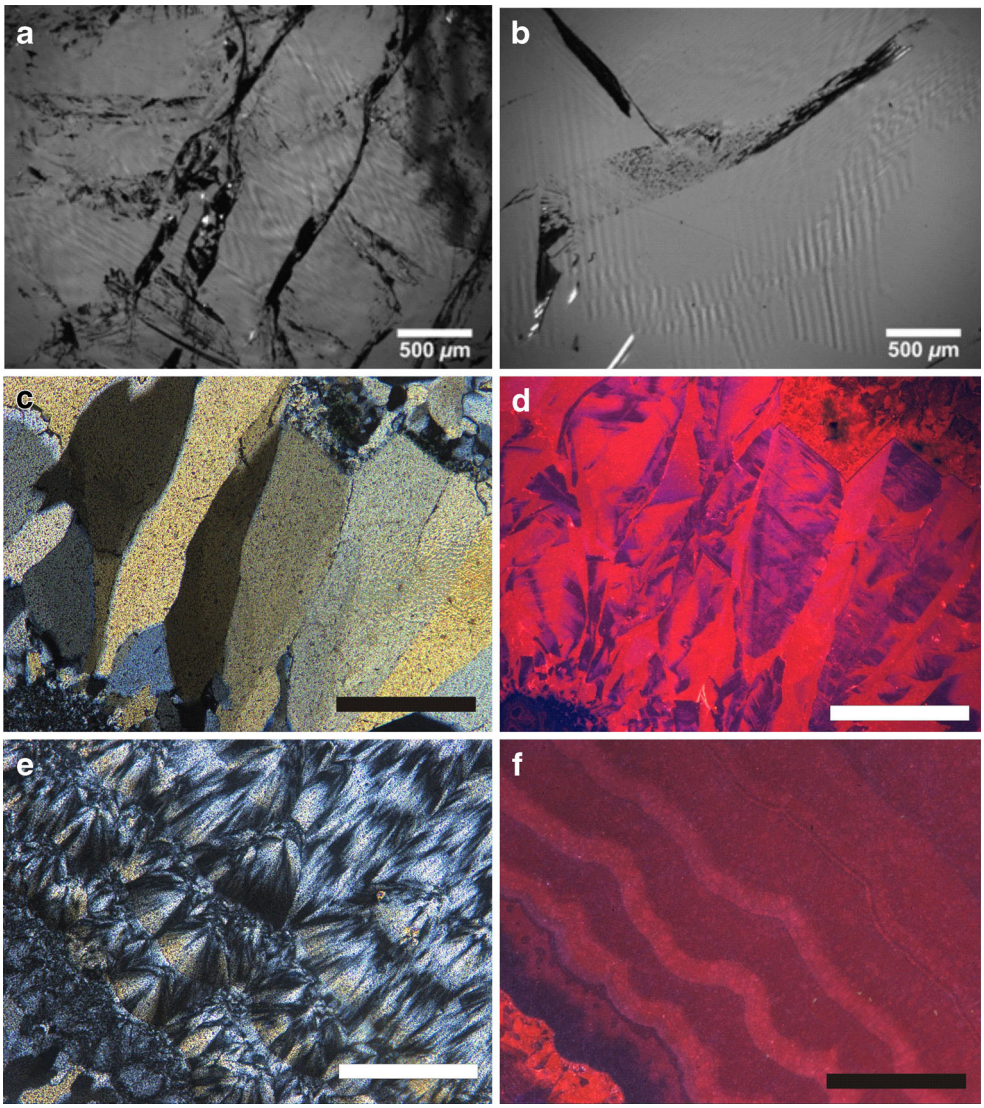

Fig. 4 Photomicrographs of textures in silica. **a** and **b** Patterns of stress-induced birefringence indicating Brazil twinning and (pseudo-)secondary fluid inclusions in thick section of amethyst sample 15335 (cross-polarized light). **c** cross-polarized light and **d** CL microphotograph of colourless and amethystine quartz showing sector zoning (sample 15253). **e** crossed polarized light and **f** CL microphotograph of chalcedony (sample 15289)

species that cause a depression of the temperature of maximum density (TMD) of the aqueous solutions. Thus, the measured T_h-T_{hr} pairs hold additional information on the salinity of the trapped solutions. To our knowledge, this is the first study that uses T_h-T_{hr} data as an independent measure for fluid inclusion salinities.

In addition, we measured ice-melting temperatures ($T_m$ice) to determine the salinity of the inclusions based on the melting point depression of the salt solutions. In order to measure $T_m$ice under equilibrium conditions we used the femtosecond laser to generate a stable vapour bubble some tenths of a degree below the final ice-melting temperature.

Salinity

The ice-melting temperatures of the inclusions range from −0.1 to −4.8 °C, corresponding to a salinity of the aqueous solutions of up to 7.6 wt% NaCl-equivalent (Bodnar 1993). The distribution of the $T_m$ice values shown in Fig. 5 displays three modes that allow us to discriminate three major fluid types (generations) based on the salinity of the solutions. The individual fluid types always occur in separate inclusion assemblages. The differentiation of individual fluid types appears even more pronounced in the T_h vs. T_{hr} diagram shown in Fig. 6, revealing a further discrimination between type 2a and type 2b inclusions (also indicated in Fig. 5). The latter, however, were only found in quartz crystals from Mioto where they supersede the type 2a inclusions. The T_h-T_{hr} measurements from low-saline type 4 inclusions seem to indicate a TMD of the aqueous solution higher than 4.0 °C, since the values plot on the left hand side of the isochoric pure water curve that was calculated from the IAPWS-95 formulation (Wagner and Pruß 2002). The real cause, however, is a systematic shift of the T_h-T_{hr} pairs to higher values due the temperature-dependent volume change of the host mineral, i.e. the non-isochoric behaviour of the inclusions, as illustrated

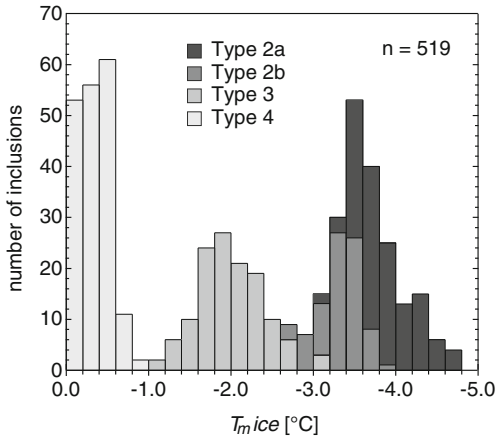

Fig. 5 Histogram of fluid inclusion ice-melting temperatures ($T_m$ice) indicating three fluid types with different salt concentrations. The differentiation between type 2a and type 2b fluids results from the T_h-T_{hr} measurements (see Fig. 6). The three fluid types can be assigned to particular mineral phases and characterise the different mineralisation stages (II to IV) of the geode infill

in the p-T diagram shown in Fig. 7. Marti et al. (2009) have demonstrated that the temperature where T_h equals T_{hr}, i.e., the starting point of the T_h-T_{hr} curve, is shifted to higher temperatures, depending on the host mineral. For the isochoric pure water system T_h equals T_{hr} at the temperature of maximum density, at 4.0 °C, while for pure water inclusions in calcite, quartz or gypsum T_h and T_{hr} become equal at 5.1, 6.1 and 8.3 °C, respectively. Thus, to determine the TMD of the

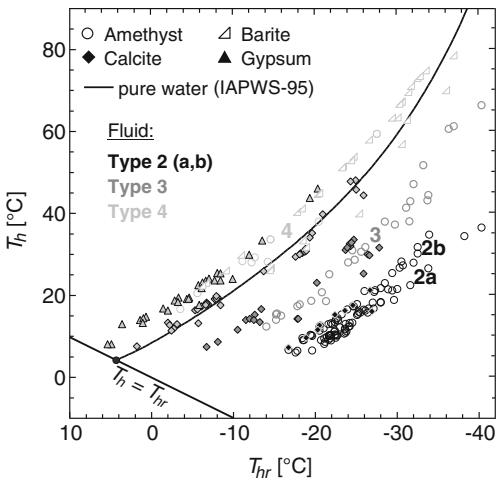

Fig. 6 T_h -T_{hr} diagram showing prograde and retrograde liquid–vapour homogenisation temperatures of fluid inclusions in quartz/amethyst (*circles*), calcite (*diamonds*), gypsum (*solid triangles*), and barite (*open triangles*). The T_h-T_{hr} data allow for a clear differentiation of fluid types (2a, 2b, 3 and 4). The solid curve illustrates the T_h-T_{hr} trend of the isochoric pure water system calculated using the IAPWS-95 formulation. The curve starts at 4.0 °C, the Temperature of Maximum Density (TMD). In an isochoric system T_h equals T_{hr} at the TMD. Although, the measured T_h-T_{hr} pairs are shifted from the isochoric pure water system due the salinity-dependent depression of the TMD and the non-isochoric behaviour of the inclusions (see Fig. 7), the data points describe a trend that is very similar to the calculated pure water curve

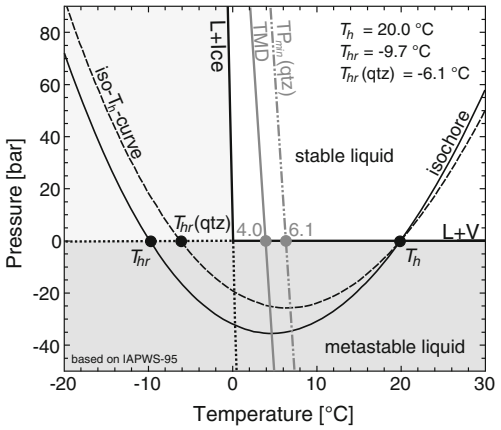

Fig. 7 Detail of the phase diagram of pure water illustrating the increase of T_{hr} due to the temperature-dependent volume change of the quartz host. *Black solid lines* liquid–vapour saturation curve (L+V) and liquid-ice coexistence curve (L+Ice). *Black dotted lines* metastable extensions of the L+V and L+Ice curves. The region of the thermodynamically stable liquid is shown in white, whereas the *grey-shaded* areas indicate the region of metastable liquid states. The liquid isochore (solid curve) shown intersects the L+V curve twice, first at T_h=20 °C and a second time at T_{hr} =−9.7 °C. For the corresponding iso-T_h curve (dashed curve) that accounts for the temperature-dependent volume change of the quartz host, T_{hr}(qtz) is at –6.1 °C, i.e., 3.6 ° greater than for the isochoric system. Note that the pressure in the inclusions is negative between T_h and T_{hr}, which means that the metastable liquid is stretched, i.e., under tensile stress. The TMD line (solid grey line) runs through the pressure minima of the isochores and intersects the L+V curve at 4.0 °C. In the non-isochoric system the Temperature of minimum Pressure line (TP_{min}; *grey dash-dotted line*) intersects the L+V curve at 6.1 °C. In the isochoric pure water system T_h and T_{hr} become equal at 4.0 °C, while for pure water inclusions in quartz the two homogenisation temperatures become equal at 6.1 °C

solution, we had to apply a mineral-specific correction to the measured T_h-T_{hr} pairs. Assuming that the addition of salt does not significantly affect the shape of the pure water T_h-T_{hr} curve, we have determined the TMD and finally, the salinity of the aqueous solutions for each T_h-T_{hr} pair using experimental data from the literature (e.g. Despretz 1840; Wright 1919; Cawley et al. 2006, and compiled values published in the International Critical Tables 1928).

Figure 8 shows the salt concentrations (in wt% NaCl-equivalent) derived from the T_h-T_{hr} data and compares them with the results obtained from the $T_m$ice measurements. The results of the two approaches can differ significantly, but they do not differ systematically. For type 2a and type 2b inclusion and, less pronounced, also for type 3 inclusions, we observe that the $T_m$ice measurements tend to result in slightly higher salt concentration and a larger variation of the data compared to the results from the T_h-T_{hr} pairs. A detailed analysis of the data revealed that the different salt concentrations cannot be explained simply by variations of the salt composition. It rather seems that the smaller salinity variations determined from the T_h-T_{hr} measurements points to inconsistencies concerning the interpretation of the ice-melting temperatures, e.g. due the presence of an undetected hydrate phase.

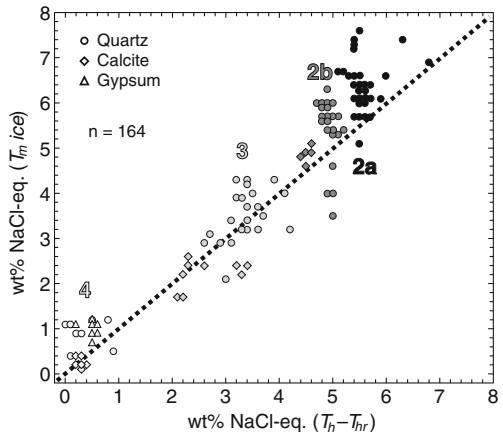

Fig. 8 Comparison of fluid inclusion salinities (concentrations in wt% NaCl-equivalent) calculated from $T_m$ice and T_h-T_{hr} data. The data points are identified by *symbols* for the different host minerals and by *grey scale* for the different fluid types. Inclusions plotting on the dotted 1:1 line yield the same salt concentrations with both methods. The diagram shows that the salt concentrations derived from $T_m$ice measurements tend to be slightly higher, particularly in type 2 inclusions

Raman spectroscopic analysis of type 2 and type 3 inclusions in quartz display a Raman band at 981 cm^{-1} that is characteristic for the vibrational mode (ν_1) of SO_4^{2-} (Fig. 9). We assume that this Raman band is attributed to substantial amounts of dissolved sodium sulphate [$Na_2SO_{4(aq)}$] in the inclusions that in some of the inclusions potentially formed a hydrate phase ($Na_2SO_4 \cdot 10H_2O$) at low temperatures. On the other hand, we could not detect any gases in the vapour bubble, such as CO_2, CH_4 or N_2 and we may describe the trapped fluids as "gas-free" aqueous salt solutions.

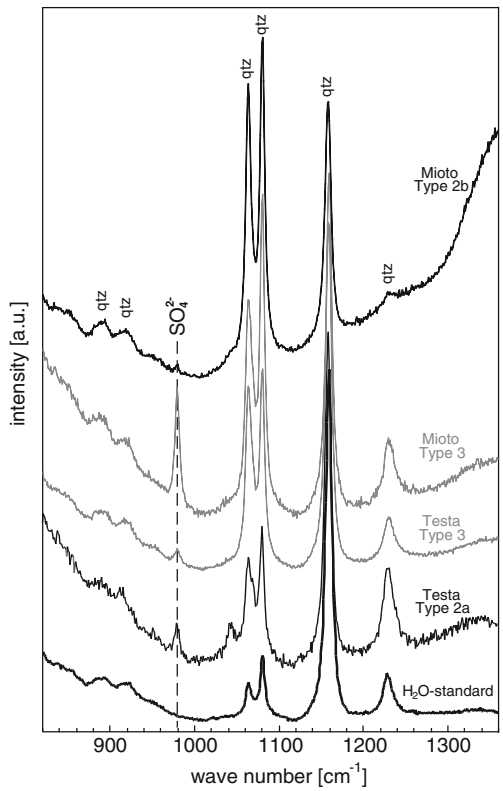

Fig. 9 Raman spectra of four fluid inclusions (type 2 and type 3) in quartz/amethyst showing the characteristic SO_4^{2-} Raman bands at 981 cm^{-1}. The Raman spectrum of a pure water inclusion in synthetic quartz is shown for comparison. The peak at 1,042 cm^{-1} in the spectrum of the type 2a inclusion from Testa is attributed to the amethyst host

We use the salinities obtained from the TMD of the aqueous solutions to distinguish the different fluid types (generations). We recall that we do not have any information from fluid inclusions on the earliest type 1 fluids that were involved in the stage I mineralisation. For the subsequent mineralisation stages, however, the characteristic fluid salinities are: 5.3–5.8 wt% NaCl-equivalent for type 2a fluids, 4.7–5.2 wt% NaCl-equivalent for type 2b fluids, 3.0–3.8 wt% NaCl-equivalent for type 3 fluids and 0.1–0.6 wt% NaCl-equivalent for type 4 fluids. Note that the salinities of type 2 and type 3 inclusions in calcite are slightly lower, than those for inclusions in quartz.

The type 2 fluid is considered to represent the oldest generation of mineralizing fluids in the geodes that is preserved in fluid inclusions. Type 2 inclusions occur only in colourless quartz and amethyst associated with stage II of the paragenetic sequence and in the early calcite that presumably formed at the transition between stages I and II. The type 3 fluid, on the other hand, is characteristic for the first generation of subhedral calcites (stage III). Type 3 inclusions also occur in quartz and amethyst, but typically along healed secondary fractures. The type 4 fluid, finally, is involved in the mineralisation of the second generation of subhedral calcite, of gypsum and rare barite (stage IV).

From these observations, we can infer that the salinity of the mineralising solutions decreased from stage II to stage IV of the paragenetic sequence. Although the record of fluid inclusions rather suggests a discontinuous fluid evolution, we note that the fluid inclusions might provide only an incomplete record of a continuous salinity decrease.

Homogenisation temperatures

Prograde T_h values of the three fluid types are shown in Fig. 10 and are illustrated in separate histograms for each host mineral. The T_h values of initially monophase fluid inclusions in quartz/amethyst display a large scatter between 7 and 138 °C that is independent of the fluid type and no differences were observed between colourless and amethystine quartz. T_h values obtained from rare two-phase inclusions typically range between 95 and 130 °C, and thus, are not greater than those measured from monophase inclusions. Note that the T_h values reported in this paper are not corrected for the effect of surface tension (Fall et al. 2009; Marti et al. 2012). The effect of surface tension on the measured T_h values becomes larger with decreasing inclusion size and increasing fluid density.

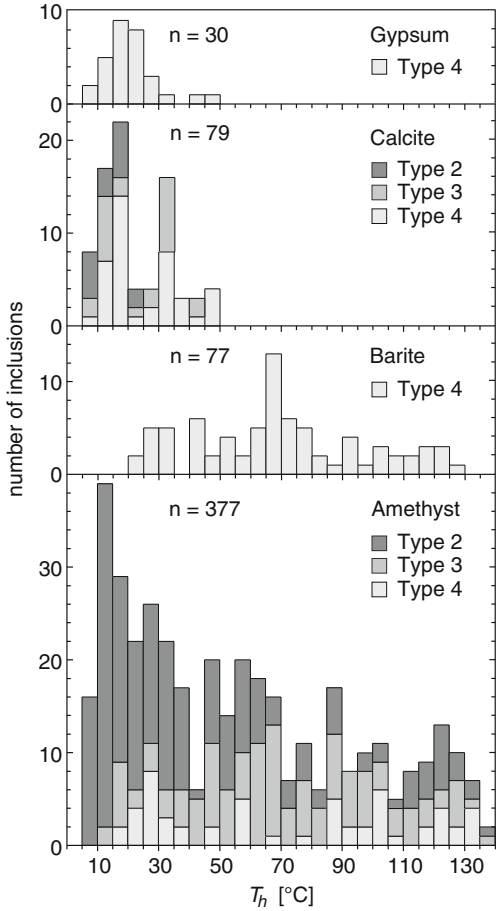

Fig. 10 Distribution of prograde homogenisation temperatures T_h arranged according to the host mineral and classified into fluid types (see text for details)

Thus, the inclusions with low homogenisation temperatures are most affected by the surface tension effect and a correction would increase these T_h values by up to 5 °C, depending on the inclusion size and the salinity.

The T_h data of type 2 inclusions in quartz and amethyst display a cluster below 40 °C with a clear mode around 12 °C and a continuous decrease of frequencies towards higher temperatures. In contrast, type 3 inclusions display a more symmetric distribution of T_h with a broad maximum around 65 °C. Type 4 inclusions finally, seem to display a weak mode at around 25 °C and a large variation of T_h towards higher temperatures. The number of type 4 inclusions in quartz and amethyst, however, is small.

The large variation of T_h of up to 120 °C in colourless quartz and amethyst is supposed to partly result from post-entrapment volume alterations of the inclusions induced by internal stress in the crystals lattice that arises from Brazil twinning (e.g. Audétat and Günther 1999). Figure 4a, b illustrate the characteristic patterns of the stress-induced birefringence in the quartz crystals viewed between crossed polarisers. In some pseudo-secondary and secondary assemblages, we observed a decrease of the T_h values from the rim to the centre of the healed fracture planes, which might result from a relaxation of the internal stress in the central part of the healed fractures. Alternatively, the decrease of T_h could also reflect the cooling of the fluid during the healing process of the open cracks.

The first generation of subhedral calcite (stage III) is characterised by type 3 inclusions with T_h values typically below 35 °C (see also Fig. 11). Gypsum and the second generation of subhedral calcite (stage IV) both precipitated from a type 4 fluid. The distribution of the T_h measurements again clearly indicates low formation temperatures of the two mineral phases, with only a few values up to 50 °C.

A detailed study was performed on a calcite crystal from the Bortoluzzi mine (sample no. 15377; Fig. 9 in Gilg et al. 2003). The crystal shows a whitish translucent core with a clear rim and a drastic 15‰ drop in the $\delta^{13}C$ values across the core-rim boundary, while $\delta^{18}O$ values fluctuate only slightly (Gilg et al. 2003). Fluid inclusion data obtained in this study now demonstrate that the core of the subhedral calcite crystal has grown from a type 3 fluid, whereas the rim precipitated from a type 4 fluid (Fig. 11). Type 4 inclusions occur as primary and pseudo-secondary inclusions in the rim but sometimes also as secondary inclusions in the core. In contrast, type 3 inclusions are missing in the rim and only occur in the core. In this particular case, the T_h values of the type 3 inclusions are distinctly higher than those from type 4 inclusions, which either indicates a decrease of the calcite formation temperature between core and rim or an increase of the fluid pressure by up to 100 bar in the type 4 fluid.

Barite, finally, is a very rare mineral phase in the paragenetic sequence of the amethyst-bearing geodes and also precipitated from type 4 fluids. In contrast to gypsum and late subhedral calcite, the T_h data from barite display a large variation and a distribution similar to that observed for the type 3 inclusions in quartz and amethyst. Although we have only a few measurements of type 4 inclusions in quartz/amethyst, the T_h values also show a large variation.

Stable isotopes

Hydrogen and oxygen

The hydrogen isotope values of fluid inclusions in amethyst range from −59 to −51‰. This small variability is surprising considering the presence of three fluid types in quartz and amethyst. This means that either their deuterium content or their relative proportions in the analysed samples are almost the same. We note that hydrogen isotope data from fluid inclusions in amethyst from Artigas, Uruguay, (Table 1) show a larger scatter.

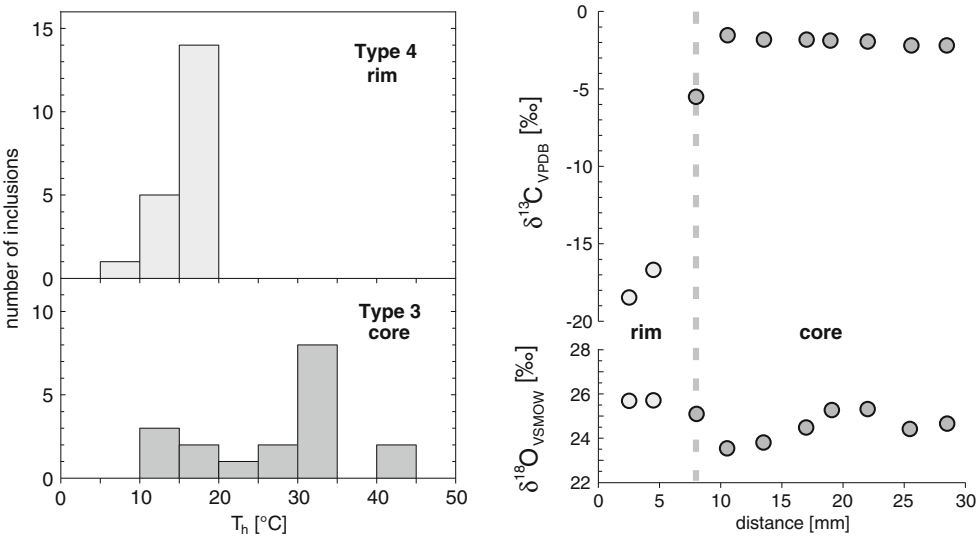

Fig. 11 Distinction between stage III and stage IV subhedral calcite. *Left panel* T_h distribution of type 3 inclusions in the core and type 4 inclusions in the rim. *Right panel* $\delta^{18}O$ and $\delta^{13}C$ profiles from the core to rim of the calcite crystal (from Gilg et al. 2003). Note the abrupt 15‰ decrease in $\delta^{13}C$ between the stage III (core) and the stage IV calcite (rim) that comes along with a compositional change of the calcite supplying fluid

The hydrogen isotope values of the fluid inclusions at Ametista do Sul are similar to the average δD_{water} values of the present-day Guaraní aquifer in São Paulo state that range from −72 to −42‰ (Silva 1983; Kimmelmann e Silva et al. 1989) with a recharge area at about 800 m above sea level. They are lighter than local meteoric waters at an elevation of about 400 m.a.s.l. (−34 to −25‰; Matsui et al. 1974). The elevation of the recharge area and the hydrogen isotope values of the Guaraní aquifer in northern Rio Grande do Sul state are the same as for São Paulo state (Kimmelmann et al. 1995).

Oxygen isotope analyses of two amethyst crystals yielded $\delta^{18}O$ values of 28.0 and 34.0‰. These new data and previously reported oxygen isotope data of Juchem (1999) and Juchem et al. (2009) suggest a significant variation of oxygen isotope values of the macrocrystalline quartz and amethyst (Fig. 12). Given that quartz and amethyst precipitated from the same type 2 fluid, the large oxygen isotope variations may be interpreted as temperature variation of at least 30 to 40 °C during the stage II mineralisation or as the result of fluid-rock interaction.

Table 1 Stable isotope results

Sample	Material	Location	$\delta^{34}S_{V\text{-}CDT}$ [‰]	$\delta D_{V\text{-}SMOW}$ [‰]	$\delta^{18}O_{V\text{-}SMOW}$ [‰]
15369	Pyrite in celadonite (geode rim)	Bortoluzzi, Ametista do Sul, Brazil	−31.5		
15344a	Pyrite in celadonite (geode rim)	ElioZanon, Ametista do Sul, Brazil	−24.6		
15344b	Pyrite in celadonite (geode rim)	ElioZanon, Ametista do Sul, Brazil	−25.4		
15834	Pyrite in chalcedony	Brazileiro, Artigas, Uruguay[c]	−33.5		
Anh-1	Pink anhydrite, silicified	Ametista do Sul, Brazil	9.9		
Anh-2	Pink anhydrite, silicified	Ametista do Sul, Brazil	9.4		
15329	platy barite	Mioto, Ametista do Sul, Brazil	7.5		
	Gypsum	various garimpos, Ametista do Sul, Brazil	5.2–6.0[b]		
15308	Gypsum	Testa, Ametista do Sul, Brazil		−63	−1.5[a]
15319	Gypsum	Testa, Ametista do Sul, Brazil		−69	−0.3[a]
15310	Amethyst	Testa, Ametista do Sul, Brazil			34.0
15276	Amethyst	Salles, Ametista do Sul, Brazil		−51	28.0
15279	Amethyst	Salles, Ametista do Sul, Brazil		−55	
15386	Amethyst	Angico, Ametista do Sul, Brazil		−59	
15829	Amethyst	Coqueiro, Artigas, Uruguay[c]		−43	
15839	Amethyst	Tarzan, Artigas, Uruguay[c]		−77	
15858	Amethyst	Berardi, Artigas, Uruguay[c]		−53	

[a] Location of the mine is found in Morteani et al. (2010)

[b] From Gilg et al. (2003)

[c] Oxygen from gypsum water

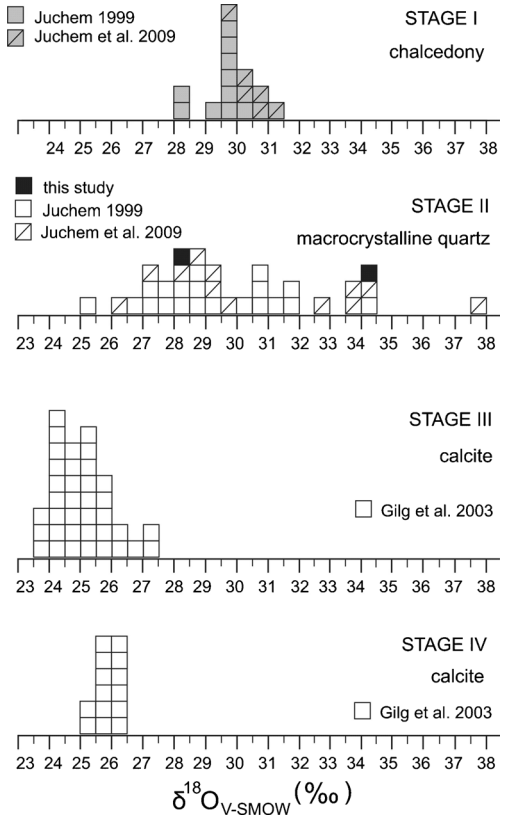

Fig. 12 Compilation of oxygen isotope values of chalcedony (stage I) and macrocrystalline colourless and amethystine quartz (stage II) and calcite (stages III and IV) from Juchem (1999), Gilg et al. (2003), Juchem et al. (2009) and this study. We note a significant oxygen isotope variation in stage II quartz

The gypsum hydration water yields δD values of −69 to −63‰ and $\delta^{18}O$ values of −1.5 to −0.3‰ (Table 1). Using the almost temperature-independent hydrogen and oxygen isotope fractionation factors between gypsum hydration water and the gypsum supplying water (Gonfiantini and Fontes 1963; Fontes and Gonfiantini 1967), the isotope composition of the gypsum supplying solution (type 4 fluid) is calculated to be −49 to −43‰ for hydrogen and −5.5 to −4.3‰ for oxygen (Fig. 14).

Sulphur

The sulphur isotope values of pyrite from Ametista do Sul range from −31.5 to −24.6‰ (Table 1). A similarly low S isotope composition of −32.5‰ is reported here for a pyrite with marcasite inclusions (Fig. 3c) from a Uruguayan amethyst deposit. Such very low sulphur isotope values are indicative for bacterial sulphate reduction (e.g. Machel et al. 1995; Ohmoto and Goldhaber 1997).

The $\delta^{34}S$ values of anhydrites range from 9.9 to 9.4‰, while $\delta^{34}S$ of a single barite sample is 7.5‰ (Table 1). The heavy isotope composition of the early sulphate phases suggests a possible involvement of modified marine sulphate. Both minerals have significantly higher sulphur isotope values than the paragenetically late gypsum (5.2 to 6.0‰, Gilg et al. 2003). The $\delta^{34}S$ values decrease in the crystallisation sequence from early to late sulphate minerals. This ca. 5‰ depletion in $\delta^{34}S$ values in the late sulphate mineralization stages could be related to increasing involvement of oxidised isotopically light sulphide sulphur.

Discussion

Microbial activity during stage I mineralisation

The very low and variable sulphur isotope composition of sulphides precipitated during stage I yields strong evidence for the activity of sulphate-reducing bacteria during the initial stage of geode infill. The reduced sulphur species might originate from bacterial sulphate reduction in the underlying sediments of the Paraná basin and be transported to the deposits. However, it appears unlikely that reduced sulphur was transported through a 1-km-thick pile of Fe^{2+}-rich basaltic rocks without reacting with them. Thus, we assume that sulphate reduction occurred within the basalts and the geodes itself.

The electron donor for the sulphate reduction is supposed to be either organic matter probably transported with the fluid from deeper parts of the sedimentary basin or hydrogen that formed through reaction of water with Fe^{2+} in the basalt (Stevens and McKinley 1995). The rarity of sulphides suggests that these electron donors were not abundant. Microbial pyrite associated with smectite, chalcedony, zeolites and even bacteriomorphs in fractures was reported in the more than 1,000 m deep meteoric aquifers in the Columbia River flood basalts and related to sulphate reduction by lithoautotrophic bacteria that used hydrogen as an electron donor (Stevens et al. 1993; Stevens and McKinley 1995; McKinley et al. 2000). The microbial pyrites in the Columbia River basalts, however, have typically a framboidal appearance (McKinley et al. 2000) and sulphur isotope fractionation is generally small for hydrogen as electron donor (Brückert 2004). Thus, we consider sulphate reduction by organotrophic bacteria more likely for the formation of sulphides at Ametista do Sul than by lithoautotrophic microorganisms.

Subsurface filamentous fabrics are common in the chalcedony of basalt-hosted amethyst and agate geodes and are interpreted as of biogenic origin (Hofmann et al. 2008). Thus, both our new sulphur isotope data and filamentous fabrics in chalcedony suggest microbial activity during the early stage I of geode infill. We recall that sulphides were not found in the subsequent mineralisation stages and apparently biogenic sulphate reduction ceased.

Temperatures of geode mineralisation

Although we have no information from fluid inclusions on the temperature and composition of the earliest type 1 fluids related to the mineralisation of celadonite, chalcedony and pyrite, indications for microbial activity yield an upper temperature limit for stage I mineralisation of about 90 to 120 °C. Sulphate-reducing microorganisms are psychrophilic to hyperthermophilic obligate anaerobes; however, their optimum growth is between 30 and 70 °C and pH near neutrality (Machel et al. 1995; Ohmoto and Goldhaber 1997). The presence of celadonite and expandable 2:1 clay minerals (saponite, nontronite) and chalcedony is consistent with this low-temperature regime (e.g. Alt 1999). The small variability of oxygen isotope compositions of chalcedony (Fig. 12; Juchem 1999; Juchem et al. 2009) suggests rather constant temperatures during the precipitation of stage I silica.

The temperature and pressure conditions during the stages II to IV of the geode mineralisation can be estimated from the T_h data of the fluid inclusions and in part from oxygen isotope data. However, the large variation of the T_h values in all three fluid types makes the interpretation of the microthermometric data challenging: The T_h distribution of the type 2 inclusions in colourless quartz and amethyst displays a clear mode between 10 and 30 °C, which indicates the presence of a high-density solution during the stage II mineralisation. This interpretation is supported by the observation that type 2 inclusion assemblages typically display a cluster of low T_h values with variations of less than 20 °C and a few values scattering up to 130 °C. In addition, we observe that the T_h values of type 2 inclusions in early stage II calcites are below 25 °C. Considering the geological context, such low T_h values can only be explained by elevated fluid pressures during quartz and amethyst precipitation, probably close to lithostatic pressure conditions. Assuming a 700–1,000-m thick overburden of basalts and possibly sediments of the Bauru Group, we can estimate a maximum fluid pressure between 210 and 290 bar. We can now apply a pressure correction to the measured T_h values by calculating the corresponding fluid isochores using the equation of state for aqueous salt solutions proposed by Mao and Duan (2008). Figure 13 illustrates that, under the given assumptions, the trapping temperature of these high-density fluid inclusions cannot be greater than 40–45 °C. Such a low formation temperature for quartz and amethyst, however, is in contradiction with the (rare) presence of anhydrite in the paragenesis of stage II. The precipitation of anhydrite from a solution with about 5 wt% NaCl requires a temperature of at least 53 °C (Hardie 1967; Blount and Dickson 1973). We therefore interpret the presence of anhydrite as a result of a short-term temperature increase in connection with tectonically induced pulses of ascending warm fluids. These upwelling fluids were not in thermal equilibrium with the host rock and gradually cooled below 45 °C after the hydrothermal event.

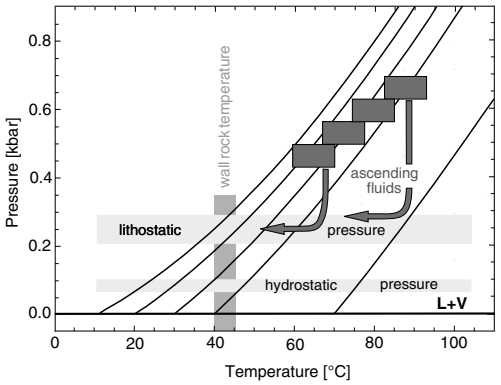

Fig. 13 P-T diagram illustrating the potential pressure and temperature conditions during stage II–IV of the geode mineralisation. L+V: liquid–vapour saturation curve (*black solid line*). Thin solid curves are liquid isochores calculated for T_h values of 10, 20, 30, 40 and 70 °C and assuming a 5 wt% NaCl solution. Light grey bars illustrate hydrostatic and lithostatic fluid pressures assuming a 700 to 1,000 m overburden at the time of the geode mineralisation. Based on this assumption, a maximum wall rock temperature between 40 and 45 °C can be estimated. Pulses of warm rapidly ascending fluids (*dark grey arrow*) from the underlying Guaraní aquifer or deeper parts of the sedimentary basin (*boxes*) are schematically illustrated (see text for details)

Furthermore, we interpret the $\delta^{18}O$ variation (26 to 34‰) of macrocrystalline quartz and amethyst as an indication for temperature variations of 30 to 40 °C during stage II, assuming a single quartz-supplying fluid of type 2 (Fig. 14). Thus, we estimate the maximum formation temperature of colourless quartz and amethyst around 80 to 90 °C.

The first generation of subhedral calcite (stage III) is characterised by type 3 inclusions with T_h values typically below 35 °C (see also Fig. 11). Thus, the formation temperature of this calcite generation is estimated to be below 45 °C. In quartz and amethyst, where type 3 inclusions occur mainly along secondary fractures, we observe a large variation of the T_h values in all of the fluid inclusion assemblages. The T_h distribution displays a broad mode around 65 °C and is completely different from the distribution pattern of the type 2 inclusions. Provided that the broad mode of the T_h values has any significance in terms of initial fluid densities, we again have to postulate an increase of the fluid temperature to at least 80 °C, which can only be caused by warm ascending fluids. Since we did not observe any high T_h values in stage III calcite and a more limited oxygen isotope variation (Fig. 12; Gilg et al. 2003), we conclude that calcite precipitated after the fluid cooled again to wall rock temperature.

Stage IV, finally, shows a similar thermal history with an initial influx of warm type 4 fluids precipitating barite and subsequent cooling of the fluid with precipitation of calcite and gypsum. The low oxygen isotope variation of stage IV calcite (Fig. 12, Gilg et al. 2003) implies constant temperatures in this final mineralization stage.

The presence of high-density fluid inclusions in quartz and amethyst, in all three generations of calcite and in gypsum

clearly demonstrates that geode mineralisation took place in a low-temperature environment with host rock temperatures below 45 °C. On the other hand, we have strong evidence from both fluid inclusions and stable oxygen isotopes for sporadic short-term temperature increases caused by repeated pulses of warm, rapidly ascending fluids that are in thermal disequilibrium with the surrounding host rock. The moderate thermal pulses could be related to periods of increased tectonic activity. The maximum temperature of these hydrothermal fluids is probably below about 80 to 90 °C (Fig. 14). This temperature range is consistent with both the occurrence of goethite and anhydrite in the stage II paragenesis. We note, however, that the postulated temperature fluctuations obviously did not cause any oscillatory growth zoning in the quartz and amethyst crystals.

Fluids and fluid sources

The origin of the early stage I fluid(s) is hitherto unknown. Anaerobic conditions during this first mineralisation stage are implied by bacterial sulphate reduction. During the subsequent deposition of macrocrystalline quartz and amethyst in stage II, the oxidation state of the fluid must have changed towards more oxidising conditions indicated by the precipitation of goethite and rarely anhydrite. The interpretation of the quartz oxygen isotope data in terms of fluid isotope composition or formation temperature strongly depends on the applied oxygen isotope fractionation between quartz and water, i.e. either using an extrapolation from high-temperature experiments (Clayton et al. 1972; Matsuhisa et al. 1978) or empirical data (Sharp and Kirschner 1994).

Assuming that the isotopic compositions of the quartz-supplying waters plot on the Global Meteoric Water Line and using the measured δD values of the fluid inclusion waters, we obtain a $\delta^{18}O$ value for the water of about −8‰. For such meteoric water, the calculated formation temperatures of quartz and amethyst would be between −2 and 26 °C using the equation of Matsuhisa et al. (1979) and between 12 and 42 °C using the equation of Sharp and Kirschner (1994). Both temperature ranges are not consistent with fluid inclusion data, the mineral paragenesis and the geological context. This result clearly indicates that the type 2 fluids must be ^{18}O-shifted from the Global Meteoric Water Line. Assuming a range of formation temperatures between 40 and 80 °C, the calculated oxygen isotope value for water in equilibrium with quartz and amethyst is about −0.8‰ using the equation of Sharp and Kirschner (1994) or +2.2‰ using the equation of Matsuhisa et al. (1979). In Fig. 14, we additionally show the fluid isotope compositions for two other temperature ranges, i.e. 20 to 50 °C and 30 to 65 °C using the Sharp and Kirschner (1994) fractionation equation. We note that the observed salt contents of the type 2 fluids do not affect this interpretation significantly (e.g. Chacko et al. 2001). In all these scenarios, the quartz- and amethyst-precipitating fluid is significantly enriched in ^{18}O compared to the present-day oxygen isotope composition of waters in the Guaraní aquifer ranging from −10.1 to -6.5‰ (Silva 1983; Kimmelmann et al. 1995; Gastmanns et al. 2010). Thus, the calculated oxygen isotope compositions of the amethyst-forming fluid are not consistent with an unmodified meteoric water composition as it is found in the Guaraní aquifer today.

The salinity of the type 2 fluid that precipitates quartz and amethyst is between 4.7 and 5.8 wt% NaCl-equivalent with significant sulphate contents. Dissolved sulphate was also detected in type 3 inclusions that show slightly lower salinities between 3.0 and 3.8 wt% NaCl-equivalent. Such salt concentrations are not known from the present-day upper Guaraní aquifer that directly underlies the Paraná basalts (e.g. Araújo et al. 1999; Meng and Maynard 2001; Pesce 2002; Sracek and Hirata 2002; Gastmanns et al. 2010). Two scenarios for the source of the type 2 and type 3 fluids can be envisaged: (a) meteoric ground waters that leached the soluble compounds from the aeolian Botucatu sandstones of the upper Guaraní aquifer during the initial phase of aquifer formation or (b) injections of sedimentary brines from deeper parts of the aquifer system. The observed systematic decrease of the fluid salinity from stage II to stage IV of the geode mineralisation and the oxidising conditions might favour the first hypothesis. However, the ^{18}O-shift of the amethyst-depositing fluid is not consistent with pure meteoric waters that leached salts from sandstones and rather suggests deep sedimentary fluids that underwent a more pronounced water-rock interaction. We note that in Argentina, for instance, salinities of up to 1.2 wt.% total dissolved salts were measured in artesian thermal waters from the lower Palaeozoic aquifer horizon that contains marine sediments (Pesce 2002). These waters are of the sodium-chloride-sulphate type and may contain high

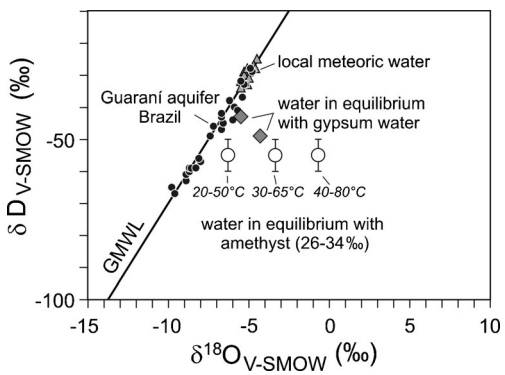

Fig. 14 δD - $\delta^{18}O$ plot showing the isotope compositions of the quartz-supplying water (open circles) calculated for various temperature ranges using the fractionation equation of Sharp and Kirschner (1994) and of the gypsum supplying fluid in equilibrium with gypsum water (*diamonds*). The isotope compositions of local meteoric waters (*triangles*; Matsui et al. 1974) and of waters in the Guaraní aquifer system from Rio Grande do Sul, Santa Catarina, Paraná and São Paulo state (*black small circles*; Kimmelmann e Silva et al. 1989) are shown for comparison and plot on the Global Meteoric Water Line (GMWL)

fluoride contents (Montaño et al. 1998; Pesce 2002). Sodium-chloride-sulphate type waters with lower salinities are also known in some parts of the uppermost Botucatu aquifer in the Brazilian sector and were generally interpreted as influx of brines from deeper aquifers (Kimmelmann e Silva et al. 1989; Meng and Maynard 2001; Sracek and Hirata 2002; Gastmanns et al. 2010). Our data demonstrate that type 2 and type 3 fluids are chloride-sulphate-bearing waters with a pronounced shift in ^{18}O. Furthermore, we interpret the high $\delta^{34}S$ values of the sulphates as an indication for modified seawater derived from marine sediments. These new results imply repeated injections of sedimentary brines from deeper levels of the sedimentary basin into the uppermost Guarani aquifer and the overlying basalts. Thus, the meteoric fluid flow model proposed by Gilg et al. (2003) is challenged and needs modification.

The source of the type 4 fluid related to the final mineralisation stage IV is probably meteoric water. The salinity is very low and the isotopic compositions calculated for the gypsum supplying type 4 fluid plot close to the local meteoric water composition (Fig. 14). This meteoric water was either descending from top through an open fluid system or ascending from the upper level of the underlying Guaraní aquifer. The latter is more likely, because (i) the very low T_h values in calcite and gypsum can hardly be explained if we assume hydrostatic pressure conditions (see Fig. 13) and (ii) the postulated temperature increase for barite precipitation is inconsistent with a scenario of descending meteoric water.

Conclusions

Monophase fluid inclusions are common in minerals that formed under low-temperature conditions. The absence of the vapour phase in the inclusions is due the extensive metastability of liquid water and makes conventional microthermometric measurements impossible. The present study demonstrates the capability of femtosecond laser pulses to efficiently and repeatedly overcome the metastable fluid state, which is the key to investigate the growth conditions of low-temperature minerals forming in near-surface environments. We have shown that T_h values of initially monophase inclusions can reach up to 138 °C. In addition, the technique allows for measurements of retrograde homogenisation temperatures, as well as for measurements of ice-melting temperatures under equilibrium conditions.

The results of our study clearly demonstrate that the geode mineralisation at Ametista do Sul is a multi-stage low-temperature process involving different fluid generations and significant changes in the oxidation state of the fluids and moderate temperature fluctuations between 40 and 90 °C that are interpreted as pulses of warm ascending fluids, probably in conjunction with tectonic activity. The mineralising fluids likely originate from different levels in the sedimentary basin underlying the basalts of the Serra Geral Formation.

The present study represents a further important step towards a comprehensive understanding of the processes that resulted in the formation of the world-class amethyst deposits in Ametista do Sul, Brazil. However, further investigations are definitely needed (i) to better constrain the timing of the geode mineralisation and duration of the individual stages, (ii) to analyse the salt composition of the fluids, e.g. by means of low-temperature Raman spectroscopy, crush-leach techniques and/or LA-ICP-MS analyses, and (iii) to determine the isotope composition of individual fluid inclusion generations, for example using wavelength-scanned cavity ring-down spectroscopy (Affolter et al. 2014).

Acknowledgments The authors thank Dr. N. Scherrer from HKB (Bern, Switzerland) for providing access to the Raman facility and for assisting with the measurements. We also appreciate the discussions with Dr. D. Marti (IAP, University of Bern, Switzerland) and his assistance with the interpretation of the T_h-T_{hr} measurements. B. Steinhilber and G. Stoschek for assistance during hydrogen, oxygen and sulphur isotope measurements. The constructive and careful reviews by B. Lehmann and U. Hein are greatly acknowledged. This study was partly funded by Swiss National Science Foundation (SNSF grant no. 200021-119966).

References

Affolter S, Fleitmann D, Leuenberger M (2014) New on-line method for water isotope analysis of speleothem fluid inclusions using laser absorption spectroscopy (WS-CRDS). Clim Past Discuss 10:429–467

Araújo LM, França AB, Potter PE (1999) Hydrogeology of the Mercosul aquifer system in the Paraná and Chaco-Paraná Basins, South America, and comparison with the Navajo-Nugget aquifer system, USA. Hydrogeol J 7:317–336

Audétat A, Günther D (1999) Mobility and H_2O loss from fluid inclusions in natural quartz crystals. Contrib Mineral Petrol 137:1–14

Baatartsogt B, Schwinn G, Wagner T, Taubald H, Beitter T, Markl G (2007) Contrasting paleofluid systems in the continental basement: a fluid inclusion and stable isotope study of hydrothermal vein mineralization, Schwarzwald district, Germany. Geofluids 7:1–25

Balzer R (2003) Rio Grande do Sul, Brasilien. Landschaften – Menschen – Edle Steine. Wenzel, Marburg, pp 1–236

Baretto SB, Bittar SMB (2010) The gemstone deposits of Brazil: occurrences, production and economic impact. Bol Soc Geol Mexicana 62:123–140

Blount CW, Dickson FW (1973) Gypsum-anhydrite equilibria in systems $CaSO_4$-H_2O and $CaSO_4$-NaCl-H_2O. Am Miner 58:323–331

Bodnar RJ (1993) Revised equation and table for determining the freezing point depression of H_2O–NaCl solutions. Geochim Cosmochim Acta 57:683–684

Borget JN (1980) Contribution à l'étude de la genèse des minéralisations silicieuses associées aux roches basaltiques du nort-ouest de l'Uruguay. PhD thesis, University of Clermont-Ferrand, France, pp. 1–173

Brückert V (2004) Physiological and ecological aspects of sulfur isotope fractionation during bacterial sulfate reduction. In: Amend JP, Edwards, KJ, Lyons TW (eds) Sulfur biogeochemistry. – past and present. GSA Spec Pub 379, pp. 1-26

Cawley MF, McGlynn D, Mooney PA (2006) Measurement of the temperature of density maximum of water solutions using a convective flow technique. Int J Heat Mass Transfer 49:1763–1772

Chacko T, Cole DR, Horita J (2001) Equilibrium oxygen, hydrogen and carbon isotope fractionation factors applicable to geological systems. Rev Mineral Geochem 43:1–81

Clayton RN, O'Neil JR, Mayeda TK (1972) Oxygen isotope exchange between quartz and water. J Geophys Res 77:3057–3066

Commin-Fischer A, Berger G, Polvé M, Dubois M, Sardini P, Beaufort D, Formoso MLL (2010) Petrography and chemistry of SiO_2 filling phases in the amethyst geodes from the Serra Geral Formation deposit, Rio Grande do Sul, Brazil. J South Am Earth Sci 29:751–760

Despretz M (1840) Le maximum de densité des liquids. Ann Chim Phys 73:296–310

Duarte LC, Hartmann LA, Vasconcelos MAZ, Medeiros JTN, Theye T (2009) Epigenetic formation of amethyst-bearing geodes from Los Catalanes gemological district, Artigas, Uruguay, southern Paraná Magmatic Province. J Volcanol Geotherm Res 184:427–436

Duarte LC, Hartmann LA, Ronchi LH, Berner Z, Theye T, Massonne HJ (2011) Stable isotope and mineralogical investigation of the genesis of amethyst geodes in the Los Catalanes gemological district, Uruguay, southernmost Paraná volcanic province. Miner Depos 46:239–255

Fall A, Rimstidt JD, Bodnar RJ (2009) The effect of fluid inclusion size on determination of homogenization temperature and density of liquid-rich aqueous inclusions. Amer Mineral 94:1569–1579

Fontes JC, Gonfiantini R (1967) Fractionnement isotopique de l'hydrogène dans l'eau de crystallization de gypse. Comptes Rend Acad Sci Paris Ser II 265:4–6

Frank HT, Gomes MEB, Formoso ML (2009) Review of the areal extend and the volume of the Serra Geral Formation, Paraná Basin, South America. Pesquisas em Geociências 36:49–57

Gastmanns D, Chang KH, Hutcheon I (2010) Stable isotopes (^{2}H, ^{18}O and ^{13}C) in groundwaters from the northwestern portion of the Guarani Aquifer System (Brazil). Hydrogeol J 18:1497–1513

Giesemann A, Jäger HJ, Norman AL, Krouse HR, Brand WA (1994) Online sulfur isotope determination using an element analyzer coupled to mass spectrometer. Analyt Chem 66:2816–2819

Gilg HA (2012) In the Beginnings: The Origins of Amethyst. In: Gilg HA, Liebetrau S, Staebler G, Wilson T (eds) Amethyst—uncommon vintage. Lithographie, Denver, Co, pp 10–13

Gilg HA, Morteani G, Kostitsyn Y, Preinfalk C, Gatter I, Strieder AJ (2003) Genesis of amethyst geodes in basaltic rocks of the Serra Geral Formation (Ametista do Sul, Rio Grande do Sul, Brazil): a fluid inclusion, REE, oxygen, carbon, and Sr isotope study on basalt, quartz, and calcite. Miner Depos 38:1009–1025

Goldberg K, Garcia AJV (2000) Palaeobiogeography of the Bauru Group, a dinosaur-bearing Cretaceous unit, northeastern Paraná basin, Brazil. Cretaceous Res 21:241–254

Goldstein RH, Reynolds TJ (1994) Systematics of fluid inclusions in diagenetic minerals. SEPM Short Course 31:1–199

Gonfiantini R, Fontes JC (1963) Oxygen isotope fractionation in the water of crystallization of gypsum. Nature 200:644–646

Götze J, Plötze M, Fuchs H, Habermann D (1999) Defect structure and luminescence behaviour of agate—results of electron paramagnetic resonance (EPR) and cathodoluminescence (CL) studies. Miner Mag 63:149–163

Hardie LD (1967) The gypsum-anhydrite equilibrium at one atmosphere pressure. Am Mineral 52:171–200

Hartmann LA, Wildner W, Duarte LC, Duarte SK, Pertille J, Arena KR, Martins LC, Dias NL (2010) Geochemical and scintillometric characterization and correlation of amethyst-bearing Paraná lavas from the Quaraí and Los Catalanes districts, Brazil and Uruguay. Geol Mag 147:954–970

Hartmann LA, Duarte LC, Massonne HJ, Michelin C, Rosenstengel LM, Bergmann M, Theye T, Pertille J, Arena KR, Duarte SK, Pinto VM, Barboza EG, Rosa MLCC, Wildner W (2012a) Sequential opening and filling of cavities forming vesicles, amygdales and giant amethyst geodes in lavas from the southern Paraná volcanic province, Brazil and Uruguay. Int Geol Rev 54:1–14

Hartmann LA, Medeiros JTN, Petruzzellis LT (2012b) Numerical simulations of amethyst geode cavity formation by ballooning of altered Paraná volcanic rocks, South America. Geofluids 12:133–141

Hofmann BA, Farmer JD, von Blankenburg F, Fallick AE (2008) Subsurface filamentous fabrics: an evaluation of origins based on morphological and geochemical criteria, with implications for exopaleontology. Astrobiology 8:87–117

International Critical Tables of Numerical Data, Physics, Chemistry and Technology, vol. III, McGraw-Hill, New York, 1928

Juchem PL (1999) Mineralogia, geologia e gênese dos depósitos de Ametista da região do Alto Uruguai, Rio Grande do Sul. PhD thesis, Universidade de São Paulo, Brazil

Juchem PL, Hartmann LA, Massonne HJ, Theye T (2009) Oxygen isotope composition of amethyst and related silica minerals in volcanic rocks from the Paraná province, southern Brazil. Congr Bras Geochímica, Ouro Preto, p 6

Kimmelmann e Silva AA, Rebouças AC, Santiago MMF (1989) ^{14}C analyses of groundwater from the Botucatu aquifer system in Brazil. Radiocarbon 31:926–933

Kimmelmann AA, Forster M, Coelho R (1995) Environmental isotope and hydrogeochemical investigation of Bauru and Botucatu aquifers, Paraná Basin, Brazil. In: Isotope Hydrology Investigations in Latin America, IAEA, Vienna, IAEA-TECDOC-835, pp. 57–74

Krüger Y, Stoller P, Rička J, Frenz M (2007) Femtosecond lasers in fluid inclusion analysis: overcoming metastable phase states. European J Mineral 19:693–706

Lieber W (1985) Pseudomorphose von Quarz nach Anhydrit. Der Aufschluss 36:143–144

Machel HG, Krouse HR, Sassen R (1995) Products and distinguishing criteria of bacterial and thermochemical sulfate reduction. Applied Geochem 10:373–389

Mao S, Duan Z (2008) The P, V, T, x properties of binary aqueous chloride solutions up to T = 573 K and 100 MPa. J Chem Thermodynamics 40:1046–1063

Mariani P, Braitenberg C, Ussami N (2013) Explaining the thick crust in Paraná basin, Brazil, with satellite GOCE gravity observations. J South American Earth Sci 45:209–223

Marti D, Krüger Y, Frenz M (2009) Fluid inclusion liquid-vapour homogenization in the vicinity of the density maximum of aqueous solutions. ECROFI XX Abstract

Marti D, Krüger Y, Frenz M, Rička J (2012) The effect of surface tension on liquid–gas equilibria in isochoric systems and its application to fluid inclusions. Fluid Phase Equilibria 314:13–21

Matsuhisa Y, Goldsmith JR, Clayton RN (1978) Oxygen isotope fractionations in the system quartz-anorthite-water. Geochim Cosmochim Acta 42:1131–1140

Matsui E, Salati E, Marini OJ (1974) D/H and 18O/16O ratios in waters contained in geodes from the Basaltic Province of Rio Grande do Sul, Brazil. Geol Soc Am Bull 85:577–580

McKinley JP, Stevens TO, Westall F (2000) Microfossils and paleoenvironments in deep subsurface basalt samples. Geomicrobiology 17:43–54

McMillan K, Cross RW, Long PE (1987) Two-stage vesiculation in the Cohassett flow of the Grande Ronde Basalt, south-central Washington. Geology 15:809–812

Meng SX, Maynard JB (2001) Use of statistical analysis to formulate conceptual models of geochemical behavior: water chemical data from the Botucatu aquifer in São Paolo state, Brazil. J Hydrol 250: 78–97

Meunier A, Formoso MLL, Patrier P, Chies JO (1988) Altération hydrothermale de roches volcaniques liée à la genèse des améthystes - Bassin du Paraná - sud do Brésil. Geochim Brasiliensis 2:127–142

Montaño J, Tujchneider O, Auge M, Fili M, Paris M, D'Elía M, Pérez M, Nagy MI, Collazo P, Decoud P (1998) Acuíferos Regionales en América Latina. Sistema Acuífero Guaraní. Capítulo argentino-uruguayo. Centro de Publicationes Universidad Nacional del Litoral, Santa Fe, Argentina, p 216

Morteani G, Kostitsyn Y, Preinfalk C, Gilg HA (2010) The genesis of the amethyst geodes at Artigas (Uruguay) and the paleohydrology of the Guaraní aquifer: structural, geochemical, oxygen, carbon, strontium isotope and fluid inclusion study. Intern J Geol Sci 99:927–947

Moxon T, Petrone CM, Reed SJB (2013) Characterization and genesis of horizontal banding in Brazilian agate: an X-ray diffraction, thermogravimetric and electron microprobe study. Miner Mag 77:227–248

Müller A (2000) Cathodoluminescence and characterization of defect structures in quartz with applications to the study of granitic rocks. PhD thesis, University of Göttingen, pp. 1-222

Neuser RD, Bruhn F, Götze J, Habermann D, Richter DK (1995) Kathodolumineszenz: Methodik und Anwendung. Zbl Geol Paläont Teil I, H 1/2:287–306

O'Neil JR, Epstein S (1966) A method for oxygen isotope analysis of milligram quantities of water and some of its applications. J Geophys Res 71:4955–4961

Ohmoto H, Goldhaber MB (1997) Sulfur and carbon isotopes. In: Barnes HL (ed) Geochemistry of hydrothermal ore deposits, 3rd edn. John Wiley & Sons, New York, pp 517–611

Pesce A (2002) Thermal spas: an economic development alternative along both sides of the Uruguay river. GHC Quart Bull Geo, Heat Center Campus Drive, September 2002, pp 22–28

Pinto VM, Hartmann LA, Santos JOS, McNaughton NJ, Wildner W (2011) Zircon U–Pb geochronology from the Paraná bimodal volcanic province support a brief eruptive cycle at ~135 Ma. Chem Geol 281:93–102

Pöllmann H (2010) Kugelfluorit auf Amethyst aus Rio Grande do Sul/Brasilien. Der Aufschluss 61:321–323

Proust D, Fontaine C (2007a) Amethyst-bearing lava flows in the Paraná Basin (Rio Grande do Sul, Brazil): cooling, vesiculation and formation of the geodic cavities. Geol Mag 144:53–65

Proust D, Fontaine C (2007b) Amethyst geodes in the basaltic flow from Triz quarry at Ametista do Sul (Rio Grande do Sul, Brazil): magmatic source of silica for the amethyst crystallizations. Geol Mag 144:731–740

Rosenstengel LM, Hartmann LA (2012) Geochemical stratigraphy of lavas and fault-block structures in the Ametista do Sul geode mining district, Paraná volcanic province, southern Brazil. Ore Geol Rev 48: 332–348

Rossman GR (1994) Colored varieties of the silica minerals. Rev Mineral 29:433–467

Sharp ZD (1990) A laser-based microanalytical method for the in situ determination of oxygen isotope ratios of silicates and oxides. Geochim Cosmochim Acta 54:1353–1357

Sharp ZD, Kirschner DL (1994) Quartz-calcite oxygen isotope thermometry; a calibration based on natural isotopic variations. Geochim Cosmochim Acta 58:4491–4501

Silva RBG (1983) Hydrogeochemical and isotopic study of groundwater of the Botucatu Aquifer, in São Paulo state (in Portuguese). PhD thesis, University of São Paulo, Brazil

Sracek O, Hirata R (2002) Geochemical and stable isotopic evolution of the Guaraní acquifer system in the State of São Paulo, Brazil. Hydrogeol J 10:643–655

Stevens TO, McKinley JP (1995) Lithoautotrophic microbia, ecosystems in deep basalt aquifers. Science 270:450–454

Stevens TO, McKinley JP, Fredrickson JK (1993) Bacteria associated with deep, alkaline, anaerobic groundwaters in southeast Washington. Microb Ecol 25:35–50

Stewart K, Turner S, Kelley S, Hawkesworth CJ, Kirstein L, Mantovani M (1996) 3-D, ^{40}Ar-^{39}Ar geochronology in the Paraná continental flood basalt province. Earth Planet Sci Lett 143:95–109

Thiede DS, Vasconcelos PM (2010) Paraná flood basalts: rapid extrusion hypothesis confirmed by new ^{40}Ar/^{39}Ar results. Geology 38:747–750

Thordarson T, Self S (1998) The Roza Member, Columbia River Basalt Group: a gigantic pahoehoe lava flow field formed by endogenous processes? J Geophys Res 103:27,411–27,445

Thordarson T, Sigmarsson O (2009) Effusive activity in the 1963–1967 Surtsey eruption, Iceland: flow emplacement and growth of small lava shields. In: Thordarson T, Self S, Larsen G, Rowland SK, Hoskuldsson A (eds) Studies in volcanology: the legacy of George Walker. Special Publications of IAVCEI 2, Geological Society, London, pp 53–84

Turner S, Relegous M, Hawkesworth CJ, Mantovani M (1994) Magmatism and continental break-up in the South Atlantic: high precision ^{40}Ar-^{39}Ar geochronology. Earth Planet Sci Lett 121:333–348

Vasconcelos PM (1998) ^{40}Ar/^{39}Ar dating of celadonite and the formation of amethyst geodes in the Paraná Continental Flood Basalt Province. AGU 1998 fall meeting, San Francisco, F933 (abs)

Wagner W, Pruß A (2002) The IAPWS formulation 1995 for the thermodynamic properties of ordinary water substance for general and scientific use. J Phys Chem Ref Data 31:387–535

Wright R (1919) The effect of some simple electrolytes on the temperature of maximum density of water. J Chem Soc 115:119–126

Zalan PV, Wolf S, Astolfi MAM, Vieira IS, Conceição JC, Appi VT, Santos Neto EV, Cerqueira JR, Marques A (1991) The Paraná Basin, Brazil. In: Leighton MW, Kolata DR, Oltz DF, Eidel JJ (eds) Interior cratonic basins. AAPG Memoir 51, pp. 681–708